Available online at www.sciencedirect.com

ScienceDirect

Scripta Materialia 92 (2014) 19–22

Scripta MATERIALIA

www.elsevier.com/locate/scriptamat

The influence of silicon and aluminum alloying on the lattice parameter and stacking fault energy of austenitic steel

G.R. Lehnhoff,[a] K.O. Findley[a,*] and B.C. De Cooman[b]

[a] *Advanced Steel Processing and Products Research Center, George S. Ansell Department of Metallurgical and Materials Engineering, Colorado School of Mines Golden, CO, USA*

[b] *Graduate Institute of Ferrous Technology, Pohang University of Science and Technology, Pohang, Republic of Korea*

Received 25 March 2014; revised 25 July 2014; accepted 28 July 2014
Available online 27 August 2014

The influence of Si and Al on the lattice parameter and stacking fault energy (SFE) of austenitic steel was studied. X-ray diffraction indicated that 2.5 wt.% Al alloying increased the austenite lattice parameter by 1.41×10^{-3} nm, whereas 2.5 wt.% Si alloying had little effect. Partial dislocation separation measurements from weak-beam dark-field images indicated that 2.5 wt.% Al alloying increased the SFE by 12–17 mJ m^{-2} and 2.5 wt.% Si alloying decreased the SFE by 6–7 mJ m^{-2}.

Keywords: Metastable austenitic steel; Stacking fault energy; Transmission electron microscopy (TEM); Lattice parameter

Advanced high-strength steels (AHSS) containing metastable austenite are candidate materials for automobile weight reduction [1–8]. Recent investigations regarding TRIP steels have evaluated the substitution of Al for Si alloying. Both Si and Al inhibit carbide formation during austempering and promote austenite retention, but Al alloying accelerates bainitic transformation during austempering [9,10] and results in better coatability [11,12]. Al alloying in TRIP steels also increases resistance to strain-induced α′ martensitic transformation relative to Si-alloyed grades [13,14] possibly due to increases in carbon partitioning to austenite during austempering [14,15] and increases in austenite stacking fault energy (SFE) [13]. This paper focuses on the effects of Al and Si alloying on the measured austenite carbon content and SFE.

Carbon is a potent austenite stabilizer, and its concentration in retained austenite is commonly ascertained by X-ray diffraction (XRD) measurements. Linear correlations between austenite lattice parameter (a_o) and carbon content are proposed in the literature [16–19]. However, Al is also reported to expand the austenite lattice [16], but its influence is sometimes excluded when calculating the austenite C content. Thus, the austenite C content in Al-alloyed AHSS may be overestimated, which steels, and thus may be misleading with regard to the effect of Al on carbon partitioning to austenite. In contrast, Si is reported to have a negligible influence on the austenite lattice parameter [16].

The SFE also affects austenite stability through its effect on shear band formation [20]. Al alloying may stabilize austenite by increasing the austenite SFE [21–24]. Experimental transmission electron microscopy (TEM) [25] and XRD [26–28] studies indicate that Si decreases the SFE of austenite, while thermochemical modeling indicates that Si decreases the SFE slightly [29] or that the influence of Si on the SFE is non-monotonic [21].

In this study, the influences of Si and Al on the austenite lattice parameter and SFE are investigated using the three austenitic steel compositions shown in Table 1, which were derived from a microstructure survey of the Fe–Ni–Cr–Al–Si system [30]. The compositions are all approximately the same except for variations in Al and Si alloying. The three steels were vacuum cast, homogenized for 20 h at 1200 °C, hot rolled and then annealed for 1 h at the temperatures indicated in Table 1 to achieve coarse grain sizes of approximately 140 μm.

Fully austenitic steels were employed because no assumptions regarding element partitioning in a multiphase microstructure need to be made in the XRD analysis. Furthermore, TEM analysis of dislocations for SFE determination is performed more easily with a coarse-grained single-phase microstructure. However, the assumptions and possible limitations of extending the analysis to multiphase AHSS must be acknowledged. Austenite is retained to room temperature in the experimental alloys by Ni and Cr alloying, not by carbon partitioning, as in AHSS. Therefore, to extend the results of this study to low-alloy AHSS, the effects of Si and Al on austenite characteristics are assumed to be independent of Ni and Cr alloying.

Seven coupons for XRD examination were taken from various locations in each alloy. The coupons were ground

* Corresponding author. Tel.: +1 303 273 3906; fax: +1 303 273 3016; e-mail: kfindley@mines.edu

http://dx.doi.org/10.1016/j.scriptamat.2014.07.019
1359-6462/

Table 1. Experimental steel compositions (wt.%) and solution annealing temperatures.

Alloy	C	N	Ni	Cr	Mn	Si	Al	Annealing Temp. (°C)
Base	0.028	0.0034	15.05	11.06	1.09	0.002	0.05	1040
2.5 Si	0.028	0.0036	14.99	10.98	1.10	2.50	0.06	1075
2.5 Al	0.030	0.0034	15.04	11.02	1.08	0.034	2.47	1060

to a 600 grit surface finish and then chemically polished for 20 min in a solution of 10 parts water, 10 parts hydrogen peroxide and 1 part hydrofluoric acid. A Phillips X'Pert® diffractometer with Cu K_α ($\lambda = 0.154060$ nm) radiation was used for the XRD. HighScore Plus® 3.0.5 software was used for analysis. The lattice parameters (a_0) determined from the first four austenite peaks ((111), (200), (220) and (311)) were plotted against $\cos^2\theta/\sin\theta$, and the a_0 for each specimen was determined from a linear regression extrapolation to $\theta = 90°$ [31]. The a_0 vs. $\cos^2\theta/\sin\theta$ regression analysis was weighted to favor higher angle peaks by using quadruplicate data points for (311) peaks, triplicate data points for (220) peaks, duplicate data points for (200) peaks and single data points for (111) peaks [32]. The lattice parameter for each material was then obtained by discarding the lowest and highest values of a_0, and averaging the results of the remaining five specimens.

For the SFE determination, 12.7 mm diameter cylinders of each material were machined with the cylinder axes parallel to the rolling direction. The cylinders were compressed to 5% true strain to introduce dislocations into the specimens. Thin slices were then sectioned from the cylinders at 45° from the compression axis and prepared for TEM by grinding and electropolishing with 95% acetic acid and 5% perchloric acid.

TEM investigation was performed in a Phillips CM12® TEM operating at 120 kV. For each material, grains with {111} planes nearly aligned with the plane of the foil were used for weak-beam dark-field (WBDF) imaging of dissociated dislocations [33,34]. The WBDF imaging was performed using **g**3**g** conditions with (220)-type reflections ($s_g \approx 0.22\ \text{nm}^{-1}$). Grains near a {111} orientation were selected because they had favorable slip conditions during compression and would therefore contain dislocations. Furthermore, dissociated dislocations imaged in this configuration are minimally inclined to the electron beam. Thus, the measured partial dislocation separations do not need to be corrected for 2-D image projection. The evaluated dislocations were confirmed to exist in the {111} plane approximately normal to the electron beam through $\mathbf{g}.\mathbf{b_p}$ analysis of the partial dislocations [33,34].

For each material, multiple data pairs of partial dislocation separation, d, and perfect dislocation character angle, α, were recorded along several dislocations. Figure 1 shows an example WBDF image of a dissociated dislocation in the base alloy, along with representations of d and α. As shown in Figure 1, α is the angle between the line vector and the Burgers vector, **b**, of the undissociated dislocation. Because both partial dislocations are in contrast in the condition shown and because $\mathbf{g}.\mathbf{b_p}$ analysis was performed, it is known that the **g** vector used to form the two-beam condition is parallel to the undissociated dislocation Burgers vector, **b**. The paired (d, α) data were then input into Eq. (1) [35] to calculate the SFE values for each measured data pair:

$$SFE = \frac{G|a_0|^2(2-\nu)}{48\pi(1-\nu)} \cdot \frac{1}{d} \cdot \left(1 - \frac{2\nu\cos 2\alpha}{2-\nu}\right) \quad (1)$$

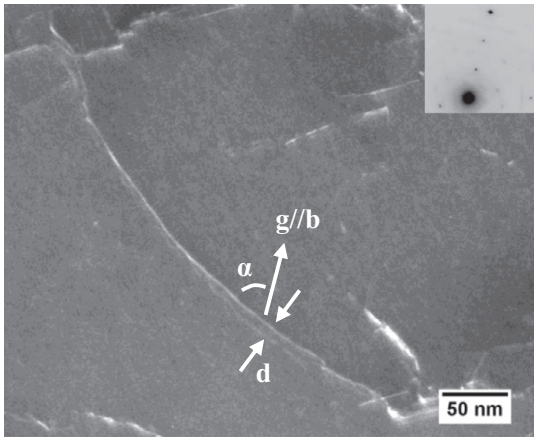

Figure 1. WBDF TEM micrograph of a dissociated dislocation in the base alloy. The annotations are explained in the text.

These values were then averaged to determine the SFE for each material. The experimental lattice parameters (a_0) determined from the XRD analysis were used in Eq. (1). The isotropic shear modulus (G) and Poisson ratio (ν) were assumed to be the same for each material, and were 74 GPa and 0.3, respectively [36]. In order to estimate the possible effect of elastic anisotropy on {111} dislocations, the effective G (66 GPa) and ν (0.43) values determined for a 12 Ni–12 Cr steel [37,38] were also applied to the experimental WBDF data, which increased the calculated SFE value for the 2.5 Al alloy by approximately 10%, but had little effect on the other two alloys. Since elastic anisotropy was not evaluated in this study and since other literature reports an effective ν closer to 0.3 instead of 0.43 [29], the isotropic elastic properties were used in the SFE calculations.

Figure 2 and Table 2 show the calculated austenite lattice parameter as a function of relative Si and Al alloying. Relative Si alloying refers to the difference in Si content between the 2.5 Si and base alloys, and the relative Al alloying refers to the difference in Al content between the two alloys. Because all of the alloys have approximately

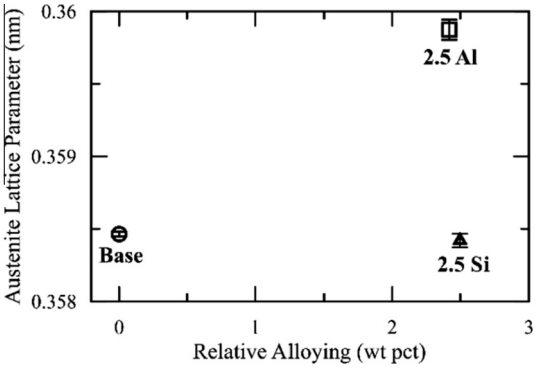

Figure 2. The dependence of austenite lattice parameter on Si and Al alloying.